ROYAL SOCIETY OF CHEMISTRY

PAPER

Check for updates

Kinetic investigation of solar chemical looping reforming of methane over Ni–CeO₂ at low temperature†

Caroline Hill, [ID] [a] Rachel Robbins,[a] Philipp Furler,[b] Simon Ackermann[b] and Jonathan Scheffe*[a]

Leveraging solar thermal energy to drive the chemical looping reforming of methane (CLRM) is a promising method of efficiently and selectively reforming methane to produce syngas using renewable energy. In this work, the role of catalytically active nickel in reaction kinetics, conversion, selectivity, and total syngas production during CLRM over Ni–CeO₂ is investigated. Through thermogravimetric analysis (TGA), metallic nickel is shown to help enhance partial oxidation of methane (POM) reaction rates as a result of a lower activation energy reaction mechanism at all oxygen nonstoichiometries, compared to CeO₂. For example, reduction rates of Ni–CeO₂ at 700 °C are comparable to CeO₂ at 900 °C, and no reaction is observed for CeO₂ at 700 °C. Further, extended cycling with Ni–CeO₂ demonstrated stable reaction rates and yields during CLRM at 700 °C, and S_{CO} remained above 0.98 for the duration of experimentation. Utilizing a larger-scale packed-bed reactor system, Ni–CeO₂ also demonstrated comparable methane conversion, syngas production and selectivity to CeO₂, but at notably lower operating temperatures, i.e., $T \leq 800$ °C. Higher rates of coking were observed during POM over Ni–CeO₂; however, all carbon was removed in the subsequent step and accumulation was not observed during extended cycling. A parametric study of gas velocity, temperature, and inlet partial pressure of methane is also presented to examine the effect these operating conditions have on conversion, selectivity, and syngas production. Notably, a tradeoff between conversion and the quantity of syngas produced was observed as gas velocity increased; however, time response of conversion indicates an ideal reaction cut-off time exists where high rates of syngas production can be achieved simultaneously with near complete methane conversion.
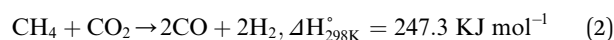
Introduction

Utilizing solar thermal energy to drive thermochemical reactions is a promising pathway for converting and storing solar energy as syngas, a mixture of CO and H₂.[1,2] Syngas serves as the precursor for production of long-chain, energy dense hydrocarbon fuels *via* well-known catalytic processes such as Fischer–Tropsch synthesis.[3,4] Catalytic methane reforming is the most widely used method for industrial syngas production and typically involves combustion of a portion of the natural gas as feedstock to provide process heat to drive the reaction.[5] This process involves the continuous delivery of CH₄ with either H₂O (steam methane reforming, or SMR) or CO₂ (dry reforming of methane, or DRM) as shown in Reaction (1) and (2), respectively.

$$CH_4 + H_2O \rightarrow CO + 3H_2, \Delta H^{\circ}_{298K} = 206.2 \text{ KJ mol}^{-1} \quad (1)$$

$$CH_4 + CO_2 \rightarrow 2CO + 2H_2, \Delta H^{\circ}_{298K} = 247.3 \text{ KJ mol}^{-1} \quad (2)$$

Both reactions are favorable at relatively low operating temperatures of 600–1000 °C, and high reaction stability and catalytic activity have been documented when noble metals such as Pt, Pd, Ru, and Rh are used as catalysts.[6–9] Notably, a solar-driven SMR reactor, where the process heat was provided by concentrated solar energy, was recently demonstrated by Zheng and Wegeng,[10] who achieved reactor efficiencies greater than 70%. Methane conversion was 80–90% at 850 °C, but deactivation due to coking reduced conversion over time. At lower temperatures of 700 °C, conversion of methane was 25–60%. Cheaper transition metal catalysts such as Ni were also utilized, however, higher loadings were required to achieve the same reactivity as noble metals.[7,11,12] Deactivation due to coke formation was also more severe over Ni, particularly during DRM.
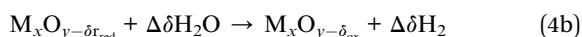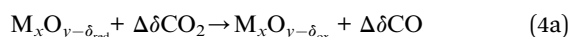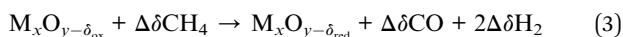
Chemical-looping reforming of methane (CLRM) is a promising but less mature pathway for producing syngas that splits

[a]Department of Mechanical and Aerospace Engineering, University of Florida, Gainesville, Florida, 32611, USA. E-mail: jscheffe@ufl.edu
[b]Synhelion SA, Lugano, 6900, Switzerland

the methane reforming process into two reactions by utilizing a nonstoichiometric metal oxide as an oxygen carrier. The two reaction steps are: (1) endothermic reduction of the metal oxide to facilitate the partial oxidation of methane (POM), followed by (2) exothermic re-oxidation of the metal oxide *via* CO_2 and/or H_2O splitting to form additional CO and/or H_2, respectively. Eqn (3) and (4) summarize these reactions for a generic metal oxide (MO) with δ representing the oxygen nonstoichiometry.

$$M_xO_{y-\delta_{ox}} + \Delta\delta CH_4 \rightarrow M_xO_{y-\delta_{red}} + \Delta\delta CO + 2\Delta\delta H_2 \quad (3)$$

$$M_xO_{y-\delta_{red}} + \Delta\delta CO_2 \rightarrow M_xO_{y-\delta_{ox}} + \Delta\delta CO \quad (4a)$$

$$M_xO_{y-\delta r_{red}} + \Delta\delta H_2O \rightarrow M_xO_{y-\delta_{ox}} + \Delta\delta H_2 \quad (4b)$$

CO_2 and H_2O splitting (Reactions (4a) and (4b), respectively) have comparable thermodynamic and kinetic favorability for reoxidation, and thus control of the H_2/CO ratio between 1 : 1 and 3 : 1 using the appropriate ratio of oxidants is possible without downstream shifting reactors.[13] The reoxidation step can also be used to remove carbon deposits formed during the POM step as additional CO.

Cerium dioxide (CeO_2) is one of the current state-of-the-art nonstoichiometric materials used for CLRM due to generally rapid redox kinetics and favorable thermodynamic properties.[14–16] CeO_2 readily reoxidizes under a wide range of conditions and maintains a stable cubic fluorite structure over a wide range of nonstoichiometry,[14,17] contributing to high oxygen exchange capacity. Scaled reactor demonstrations have proven CeO_2 is a viable redox material for CLRM at temperatures $\geq$ 1000 °C.[18,19] Notably, Fosheim *et al.*[20] utilized a prototype reactor at 1/6th capacity to demonstrate a solar-to-fuel efficiency ($\eta_{solar-to-fuel}$) of 7% at 1000 °C. Scaling to full capacity was predicted to increase $\eta_{solar-to-fuel}$ to 31%, with commercial reactors reaching up to 56% due to lower thermal losses. During cycling, stable methane conversion of 36% and CO and H_2 selectivities of 82% and 90%, respectively, were observed. The highest $\eta_{solar-to-fuel}$ observed to-date for CLRM, 10.06%, was recorded by Warren *et al.*[21] in a vertical packed bed reactor operating at 1150 °C. This was achieved by optimizing a wide range of parameters, most notably controlling the non-stoichiometry range of CeO_2. Methane conversion and syngas selectivity were 69% and $\geq$93%, respectively. While these demonstrations have proven CeO_2 as a viable redox material for CLRM at temperatures $\geq$1000 °C, the slow kinetics of POM over CeO_2 below 1000 °C, which is more industrially viable, make lower temperature operation impractical.

To improve reaction rates, surface decoration of CeO_2 based redox materials with catalytic metals has been proposed. The addition of Pt and Rh to supported CeO_2, studied by Fathi *et al.*[22], enhanced methane conversion during pulse experiments at 700 °C. Similar improvement in POM activity was demonstrated by Carrillo *et al.*[23] using CeO_2 with exsolved Ru nanoparticles cycled at temperatures of 700–900 °C. Ni, Co, and Fe deposition on CeO_2 and Zr-doped CeO_2 have also been investigated by Guerrero-Caballero *et al.*,[24] with Ni decorated CeO_2 exhibiting the highest methane conversions of 65–90% at

700–800 °C. Metallic Ni has been studied as a promising catalyst candidate by others as well,[25–27] including Ouyang *et al.*[28] who conducted a detailed study of the POM reaction mechanism over Ni catalyzed CeO_2 by delivering short pulses of methane to 20 wt% Ni supported on gadolinium-doped CeO_2 at 600 °C. Results indicate the reaction proceeds by methane decomposition combined with oxidation of carbon *via* surface oxygen from CeO_2. Bulk migration of oxygen within CeO_2 was identified as the rate-determining step.

Subsequent demonstrations by Löfberg *et al.*[29] show consistent, high conversion of methane and CO_2 at low temperatures are attainable using Ni promoted CeO_2 for CLRM. Following 12 cycles at 700 °C with 8.8 wt% Ni on CeO_2, CH_4 and CO_2 conversions were ~80%. Increasing the operating temperature to 800 °C improved CH_4 and CO_2 conversions to 95% and 99%, respectively, averaged over 60 cycles. Later work by Han *et al.*[30] utilized ultralow loadings of Ni (0.1 and 1 wt%) on CeO_2 and exhibited similarly high conversions, ~99% for both CH_4 and CO_2, over 50 cycles at 900 °C. Although each of the prior studies prove the viability of CLRM over Ni enhanced CeO_2 at low temperatures, there remain considerable gaps in our understanding of the reaction chemistry. For example, none of the aforementioned studies documented the role of CeO_2 non-stoichiometry on reaction rates, conversion, and selectivity, which has been shown to have a large impact for other material systems.[21,31,32] Further, in the prior studies, reactions were only operated under a fixed set of cycling conditions (*i.e.*, gas velocity, reaction time, and partial pressure of feedstock) that produced high conversions.

In this study, we build on the previous CLRM work using Ni catalyzed CeO_2 (Ni–CeO_2) to better understand the effect of temperature and composition (*i.e.* nonstoichiometry) on kinetics, stability, and selectivity to CO and H_2 in the range 700–1100 °C. A parametric study of packed-bed reactor conditions (gas velocity, temperature, and inlet methane concentration) is also performed to understand the impact on methane conversion, syngas selectivity, and total syngas production.

Experimental section

Material synthesis and characterization

Commercial CeO_2 powder (Alfa Aesar, 11328) was employed for non-catalytic CeO_2 experiments and as the base material for synthesis of 5 wt% Ni–CeO_2 using a wetness impregnation method. For Ni–CeO_2 synthesis, the appropriate amount of nickel(II) nitrate hexahydrate (Sigma-Aldrich, 203874) was added to 10 mL of deionized water, followed by the addition of CeO_2 to the solution. The mixture was stirred for 1 hour at 300 rpm, then heated at 70 °C until dry. The resulting material was moved to an alumina boat crucible and heated in air in a Carbolite RHF 16/8 box furnace at 110 °C for 12 hours (5 °C ramp rate). The sample was subsequently ground with a mortar and pestle, then sintered for 10 hours at 1200 °C (5 °C ramp rate). The final sample was again ground with mortar and pestle before use. For an equivalent comparison of catalyzed *vs.* non-catalyzed CeO_2, commercial CeO_2 powder was also sintered under the same conditions before use in experiments. Particle

size distribution of both CeO_2 and Ni–CeO_2 powder samples was evaluated using a TSI PSD3603 Aerosizer.

Large particle (LP) CeO_2, synthesized using a method described in previous work,[21] was also used as a base material for synthesis of 5 wt% Ni–CeO_2. Synthesis of LP CeO_2 started with commercial CeO_2 powder, which was then sintered in a large diameter alumina crucible for 10 hours at 1200 °C. The resulting compacted slab was ground with a mortar and pestle and then sieved to obtain particle diameters (D_p) in the range $500 \leq D_p < 1400$ μm. Ni was added to the LP CeO_2 using a similar wetness impregnation method to the method described above, however, the sample was stirred for only 5 minutes by hand instead of 30 minutes at 300 rpm to prevent deterioration of the LP CeO_2. Grinding with mortar and pestle was also omitted. Finally, because the LP CeO_2 was sintered before the addition of Ni, the last sintering step was removed.

Powder X-ray diffraction (PXRD) patterns for LP CeO_2 and LP Ni–CeO_2 at various stages of cycling were collected using a PANalytical X'Pert Powder Diffractometer with Cu-Kα radiation and output of 45 kV/40 mA. Scans were performed under the following conditions: 0.008° step size, 15.24 s dwell time, and 2θ ranging from 20°–90°. Scanning electron microscopy (SEM) and energy-dispersive X-ray spectroscopy (EDS) elemental mapping for as-synthesized and cycled LP Ni–CeO_2 were performed on an FEI Nova NanoSEM 430 instrument with an integrated EDAX silicon drift detector.

Thermogravimetric analysis

A horizontally oriented thermogravimetric analyzer (HT TGA/DSC 2, Mettler Toledo), or TGA, was used to measure oxygen nonstoichiometry of CeO_2-based samples during redox cycling. 10 mg samples of each powder material were placed on a flat platinum plate crucible in a thin layer to minimize limitations of gaseous mass transfer. During each experiment, samples were heated to 1100 °C, purged in Ar (g) at 1 atm for 1 hour, then cycled isothermally twice at 1100 °C to ensure material stability.[31] Subsequent isothermal cycles followed a randomized temperature profile for isothermal cycling between 700 °C and 1000 °C with a 10 °C min^{-1} ramp rate between temperatures. Each isothermal cycle consisted of the following four steps: 2 min purge in Ar (g) ($\dot{V}$ = 300 sccm), reduction in CH_4 (Φ_{CH_4} = 3 vol% balanced in Ar (g), $\dot{V}$ = 300 sccm) for variable timespans but generally until a steady state mass is reached, 2 min purge in Ar (g) ($\dot{V}$ = 300 sccm), and 3 min oxidation (Φ_{CO_2} = 2 vol% balanced in Ar (g), $\dot{V}$ = 285 sccm). $\dot{V}$ and Φ indicate the volumetric flow rate and inlet concentration, respectively. To correct for buoyancy effects, a blank run with only the platinum crucible was performed under the same conditions and temperature profile following each experiment. Nonstoichiometry during reduction (δ_{red}) of the noncatalytic CeO_2 samples was calculated using eqn (5), where $\Delta m_s(t)$ is the measured change in mass starting from a fully oxidized sample, $m_{s,i}$ is the initial sample mass, M_s is the molar mass of CeO_2, and M_O the molar mass of monatomic oxygen. A similar approach was used to calculate δ_{red} of the Ni–CeO_2 materials; however, because the sample initially starts with NiO that is

reduced in the first cycle to metallic Ni, $m_{s,i}$ was taken as the sample mass immediately preceding the second reduction step and $\Delta m_s(t)$ was measured from this starting mass. The rate of change of δ_{red} (dδ/dt) was evaluated by simply taking the time derivative of $\delta_{red}(t)$.

$$\delta_{red}(t) = \frac{|\Delta m_s(t)|}{m_{s,i}} \left(\frac{M_s}{M_O} \right) \quad (5)$$

A mass spectrometer (HPR-20 QIC, Hiden Analytical) was used to measure product gas species CO, CO_2, and H_2 downstream of the TGA. Total moles of each respective gas, n_{CO}, n_{CO_2}, and n_{H_2}, were determined by integrating the molar flow rate of each species. Total moles of H_2O produced (n_{H_2O}) were calculated via a molar balance on oxygen, as shown in eqn (6). Here, n_O represents the total moles of monatomic oxygen removed, evaluated by dividing the change in sample mass by the molar mass of oxygen.

$$n_{H_2O} = n_O - (n_{CO} + 2n_{CO_2}) \quad (6)$$

Selectivity to CO (S_{CO}) and H_2 (S_{H_2}) during POM were calculated using eqn (7) and (8), respectively. Selectivities were assessed at the time reduction extent reached steady state, or after 10 min of CH_4 delivery if the POM reaction continued longer than 10 min.

$$S_{CO} = \frac{n_{CO}}{n_{CO} + n_{CO_2}} \quad (7)$$

$$S_{H_2} = \frac{n_{H_2}}{n_{H_2} + n_{H_2O}} \quad (8)$$

CLRM packed-bed reactor setup

Experiments were performed in a horizontal packed-bed reactor system modified from a prior work.[33] During each test, 1.0 grams of LP CeO_2 or LP Ni–CeO_2 were added to a 4 mm ID alumina tube and held in place with alumina fiber insulation. A horizontal tube furnace (Carbolite STF 16/180) was used to reach and maintain steady operating temperatures (T) ranging from 700–1100 °C. Inlet gas flow rate and concentration were adjusted via three mass flow controllers (MKS GE50A) connected to mixtures of Φ_{CH_4} = 10 vol% balanced in Ar (g), Φ_{CO_2} = 5 vol% balanced in Ar (g), and pure Ar (g). A condenser ice bath was placed at the exit of the furnace, prior to downstream gas analysis. Pressure was maintained at 1 atm by an absolute pressure controller (MKS Type 640B) coupled with a rotary vane vacuum pump downstream. Control of furnace temperature, gas flowrates, and pressure was achieved using an integrated custom LabVIEW VI program. Effluent gas composition was evaluated using a mass spectrometer (Stanford Research Systems QMS100) to measure partial pressure of CO_2 and H_2 and an infrared (IR) gas analyzer (Siemens Ultramat 23, uncertainty ≤1 vol% of full scale) to quantify volume percent of CH_4 and CO.

Typical CLRM cycles consisted of the following steps: (1) POM with Φ_{CH_4} = 5 vol% or 10 vol% balanced in Ar (g), (2) 10 min purge in Ar (g), (3) oxidation with Φ_{CO_2} = 5 vol%

balanced in Ar (g), followed by (4) 10 min purge in Ar (g). The length of the POM and oxidation steps were dependent on the redox material and operating conditions; however, oxidation always proceeded until evidence of reaction was complete, *i.e.* no CO was measured in the reactor effluent. $\dot{V}$ was maintained at 50, 100, or 150 sccm, corresponding to gas velocities (ν_g) of 0.068, 0.135, or 0.203 m s^{-1}, respectively. At each set of operating conditions, a 'blank' experiment with no sample in the tube was performed to obtain the time response of specific flow rates of CH_4 and CO_2 entering the reactor ($\dot{n}_{CH_4,in}$ and $\dot{n}_{CO_2,in}$).

Since total moles of converted CH_4 ($n_{CH_4,conv}$) can be quantified directly in this reactor system, eqn (9) and (10) were used to determine S_{CO} and S_{H_2}, respectively. Note that this approach accounts for carbon, unlike equations used during TGA analysis where carbon was not observed.

$$S_{CO} = \frac{n_{CO}}{n_{CH_4,conv}} \quad (9)$$

$$S_{H_2} = \frac{n_{H_2}}{2n_{CH_4,conv}} \quad (10)$$

Instantaneous methane conversion (X_{CH_4}) and average methane conversion ($\overline{X}_{CH_4}$) are described by eqn (11) and (12), respectively. Here, $\dot{n}_{CH_4,in}$ and $\dot{n}_{CH_4}$ represent the specific molar flow rate of methane entering and leaving the reactor, respectively.

$$X_{CH_4} = \frac{\dot{n}_{CH_4,in} - \dot{n}_{CH_4}}{\dot{n}_{CH_4,in}} \quad (11)$$

$$\overline{X}_{CH_4} = \int_{t_0}^{t} \frac{\dot{n}_{CH_4,in} - \dot{n}_{CH_4}}{\dot{n}_{CH_4,in}} dt \quad (12)$$

Bed averaged nonstoichiometry (δ_{avg}) was determined using eqn (13) which implements a molar balance on the oxygen containing product species. n_{H_2O} was not measured directly and was instead related to $n_{CH_4,conv}$ and n_{H_2} as shown in eqn (14).

$$\delta_{avg} = \left(\frac{M_s}{m_{s,i}}\right)(2n_{CO_2} + n_{CO} + n_{H_2O}) \quad (13)$$

$$n_{H_2O} = 2n_{CH_4,conv} - n_{H_2} \quad (14)$$

Carbon deposition during POM, also not measured directly, was evaluated *via* a molar balance on the carbon containing species as shown in eqn (15).

$$n_C = n_{CH_4,conv} - n_{CO} - n_{CO_2} \quad (15)$$

Uncertainty analysis

Uncertainty analysis using error propagation methods was completed for all performance metrics based on measurement uncertainty in each device (mass spectrometer, mass flow controllers, and IR analyzer) combined with a 95% confidence interval for all calibrations. Calibration of the mass spectrometer was completed before each experiment and corresponds to the gas pressure at the time of calibration. Thus, any drift in

pressure over the course of longer experiments may cause additional variation in the results not accounted for by the uncertainty analysis.

Results and discussion

CLRM in TGA

Exemplary TGA redox cycling results using CeO_2 and $Ni–CeO_2$ between 700 and 1100 °C are shown in Fig. 1a and b, respectively. The final cycle at 800 °C for both materials is outlined for clarity. Each decrease in mass corresponds to the POM and concurrent reduction of the redox material, whereas each sharp increase in mass corresponds to re-oxidation of the samples with CO_2. CeO_2, shown in Fig. 1a, re-oxidizes after POM to the same mass following each oxidation step. Based on thermodynamic and kinetic studies, this is assumed to be the stoichiometric state $\delta = 0$. The starting behavior of $Ni–CeO_2$, shown in Fig. 1b, is notably different. The mass declines slightly during initial heating from room temperature to 1100 °C and is followed by a decrease in mass during the first POM. However, during the subsequent oxidation with CO_2, the mass does not increase to the same initial value as it did with CeO_2. PXRD patterns for CeO_2 and $Ni–CeO_2$ at various stages, shown in Fig. S1,† indicate this discrepancy is due to NiO formed during synthesis of $Ni–CeO_2$, which is subsequently reduced to metallic Ni during the first exposure to CH_4 and then not re-oxidized upon exposure to CO_2. Therefore, the mass following the first
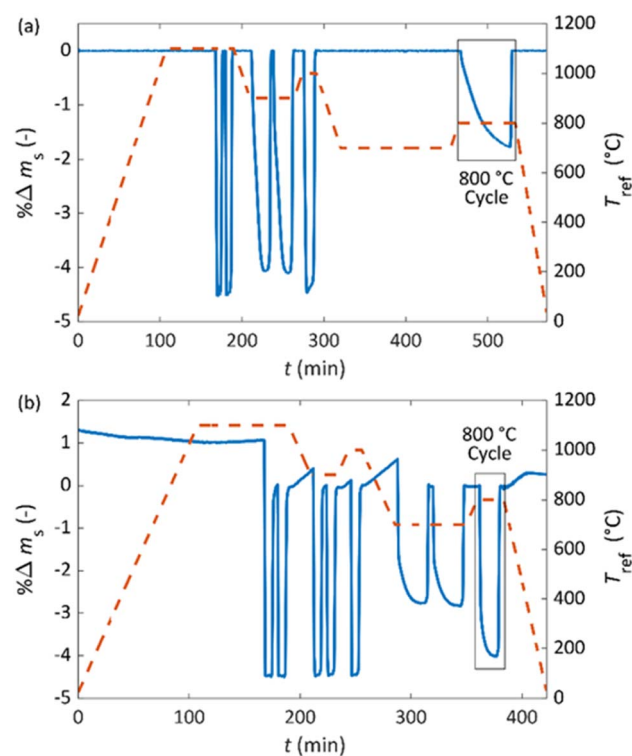

Fig. 1 %Δm_s (solid), and reference temperature, T_{ref} (dashed), as a function of time during CLRM over (a) CeO_2 and (b) $Ni–CeO_2$. A preset randomized temperature profile was used for both experiments. The final cycle at 800 °C is indicated for each material.
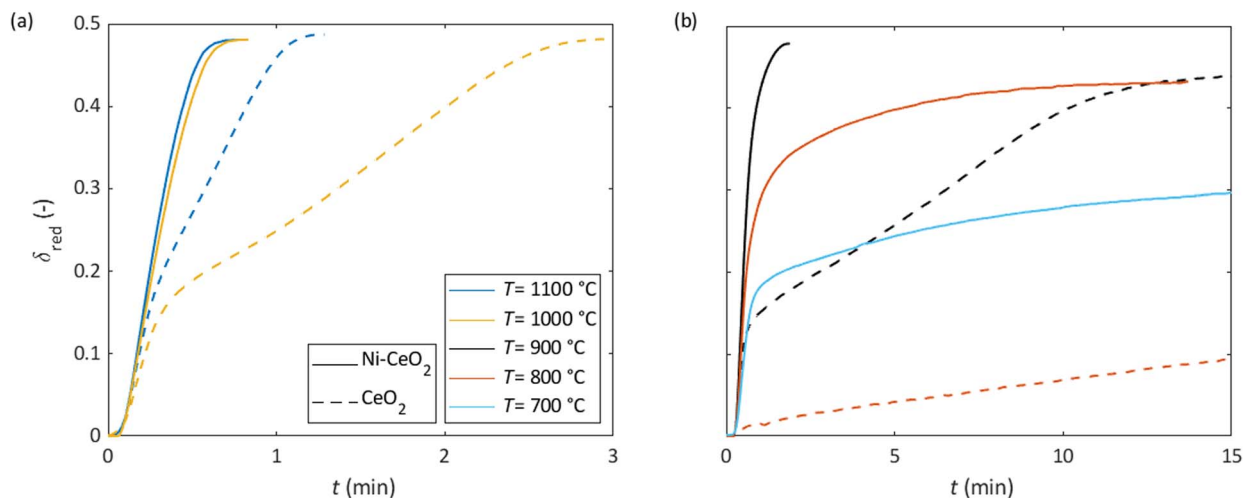
Fig. 2 δ_{red} as a function of time during POM over Ni–CeO$_2$ (solid) and CeO$_2$ (dashed). Results are grouped by temperature to show similar reaction rates on the same time scale: (a) 1100 °C and 1000 °C, and (b) 900 °C, 800 °C, and 700 °C.

oxidation is taken as the stoichiometric state $\delta = 0$ of Ni–CeO$_{2-\delta}$ and percent change in mass ($\%\Delta m_s$) is set to zero at this point. This is further corroborated by the fact that the change in mass from the start of the first cycle to the point set as $\delta = 0$ is approximately equivalent to the mass of oxygen needed to fully oxidize 5 wt% Ni to NiO. The slow and mostly linear increases in mass during temperature transitions following the rapid increases are attributed to Ni^0 oxidizing with trace amounts of O$_2$ in the purge gas.

For redox cycles at $T \geq 1000$ °C, there are no notable distinctions between Ni–CeO$_2$ and CeO$_2$ when viewed from this scale, as both materials quickly reduce during POM to reach a $\%\Delta m_s = -4.5\%$. At lower temperatures, however, $\%\Delta m_s$ is greater during POM for Ni–CeO$_2$. Notably, Ni–CeO$_2$ even reduces at 700 °C, while CeO$_2$ exhibits no appreciable change in mass under these conditions.

Exemplary results for δ_{red} as a function of time are displayed in Fig. 2. In general, most δ_{red} curves for CeO$_2$ are characterized by two distinct regions; the first is a fast reaction rate at the start of the POM reaction indicated by the steep slope in δ_{red}, followed by an inflection point after which rates are noticeably slower. This transition is not apparent for Ni–CeO$_2$ except at the lowest temperature of 700 °C. We attribute this sharp change in rates, at least in part, to the bimodal particle size distribution which is shown in Fig. S1.† On average, reduction rates were appreciably faster for Ni–CeO$_2$ samples at all operating T. At 1100 °C and 1000 °C, shown in Fig. 2a, Ni–CeO$_2$ reaches steady state δ_{red} in less than 1 min, while 1.3 and 3.0 min are required for CeO$_2$ at each respective temperature. The most dramatic differences between Ni–CeO$_2$ and CeO$_2$ are evident at $T \leq 900$ °C, shown in Fig. 2b. For example, POM rates over Ni–CeO$_2$ at 700 °C are comparable to CeO$_2$ at 900 °C, and no reaction is observed for CeO$_2$ at 700 °C. The final δ_{red} approached 0.5 for both CeO$_2$ and Ni–CeO$_2$, indicating that the presence of metallic Ni does not change the bulk oxygen exchange capacity of CeO$_2$.

The increase in POM reaction rates observed above can be partially explained by a lower apparent activation energy (E_a) for Ni–CeO$_2$ compared to CeO$_2$ over all δ_{red}, as shown in Fig. 3. Results were calculated using temperatures of 900–1100 °C in a model free approach described in prior work.[31,32] E_a for POM over CeO$_2$ at low nonstoichiometry is ~30 kJ mol^{-1} but increases to 200 kJ mol^{-1} at $\delta_{red} = 0.15$. At higher δ_{red}, E_a of CeO$_2$ varies slightly but generally remains between 165 and 215 kJ mol^{-1}. In comparison, E_a of Ni–CeO$_2$ is lower, ~20 kJ mol^{-1} at low nonstoichiometry, and remains below 50 kJ mol^{-1} until $\delta_{red} \geq 0.35$. The notable difference in E_a of each material provides evidence that the difference in rates is indeed a catalytic effect rather than because of changes in specific surface area. During computation of E_a it is assumed for ease of calculation that particle size is constant, and thus δ_{red}
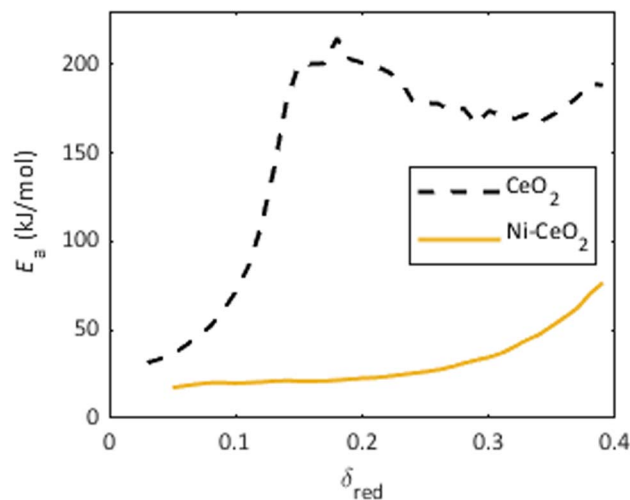

Fig. 3 E_a as a function of δ_{red} for CeO$_2$ (dashed) and Ni–CeO$_2$ (solid). Results were calculated using δ_{red} curves during POM at temperatures of 900–1100 °C.
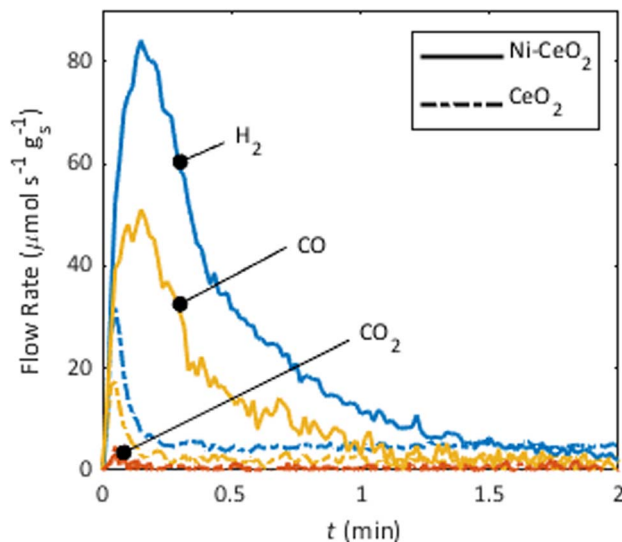
Fig. 4 $\dot{n}_{H_2}$, $\dot{n}_{CO}$, and $\dot{n}_{CO_2}$ during the POM over Ni–CeO$_2$ (solid) and CeO$_2$ (dashed) at 800 °C.

and dδ_{red}/dt are uniform for the entire sample mass. However, as shown in Fig. S2,† both CeO$_2$ and Ni–CeO$_2$ have irregular, left-skewed particle size distributions with two distinct peaks, but are not markedly different. Therefore, we expect that any deviations of this apparent activation energy from the true activation energy should affect both materials similarly.

Exemplary molar specific flow rates, $\dot{n}_i$, of measured product gas species at 800 °C, shown in Fig. 4, indicate selectivity to CO and H$_2$ are high during POM over both Ni–CeO$_2$ and CeO$_2$. CO$_2$ formation is suppressed in comparison to CO, with only minimal formation of CO$_2$ at the reaction onset for both materials. The ratio of $\dot{n}_{H_2}$ to $\dot{n}_{CO}$ is approximately 2 : 1, indicating formation of H$_2$O is also low. Further, $\dot{n}_{H_2}$ and $\dot{n}_{CO}$ are significantly greater for Ni–CeO$_2$ compared to CeO$_2$, in agreement with the gravimetric data. Similar trends are observed at all temperatures.

As illustrated in Table 1, S_{CO} in general remains high (≥ 0.96) and is equivalent for POM over CeO$_2$ and Ni–CeO$_2$ at comparable operating T. There is a slight trend of increasing S_{CO} with decreasing temperature, with selectivity approaching 1.00 during POM at $T \leq 800$ °C. This value indicates ~100% selectivity of the carbon containing product gas species to CO but does not provide any information on the amount of carbon deposited during the POM reaction. However, comparison of $\dot{n}_{CO}$ to the rate of oxygen absorption during the oxidation step, shown in Fig. S3,† exhibits approximately a 1 : 1 molar ratio, indicating no carbon is removed during oxidation. Since

oxidation of carbon with CO$_2$ is favorable under these conditions, we can assume negligible carbon deposition occurs during POM.

Similar to S_{CO}, a slight trend of increasing S_{H_2} is present as temperature decreases. This trend agrees with thermodynamic predictions of lower CO$_2$ and H$_2$O production at reduced temperatures. S_{H_2} remains high (≥ 0.90) for CeO$_2$ but is notably lower for Ni–CeO$_2$ at all temperatures, indicating higher rates of H$_2$O formation over Ni–CeO$_2$.

TGA stability analysis

Reaction rates and selectivities during POM remained stable during extended cycling of LP Ni–CeO$_2$. As shown in Fig. 5, both $\delta_{red}|_{t=20\ min}$ and dδ/d$t|_{\delta=0.1}$ are consistent over the first 120 cycles conducted at 700 °C, with average values of 0.26 (−) and 0.45 (min^{-1}), respectively. After the first 120 cycles, temperature was increased to 900 °C for 10 cycles (not shown) in order to identify if higher temperature operation accelerates de-activity. Indeed, after this point (indicated by the dashed vertical line), there is a slight decrease in $\delta_{red}|_{t=20\ min}$ and dδ/d$t|_{\delta=0.1}$ but the remaining 80 cycles at 700 °C are again stable with standard
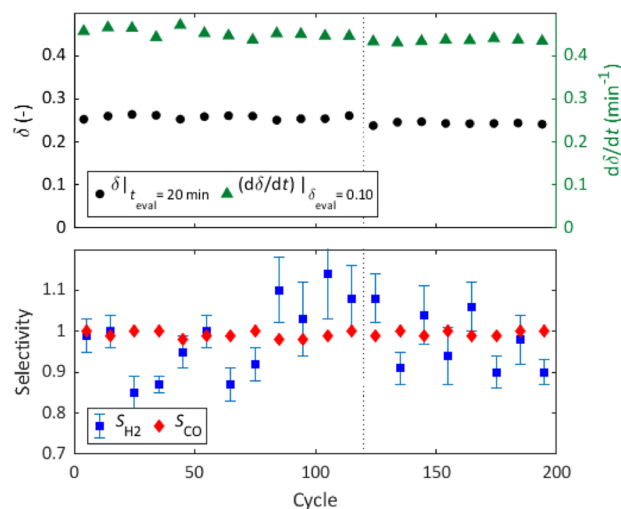

Fig. 5 A stability investigation was completed for CLRM over LP Ni–CeO$_2$ consisting of 200 cycles performed isothermally at 700 °C. Results are shown for every 10th POM reaction: (a) δ_{red} 20 min after the start of the reaction (circle) and dδ/dt evaluated at $\delta = 0.10$ (triangle), and (b) S_{CO} (diamond) and S_{H2} (square). After the first 120 cycles at 700 °C, 10 cycles were completed at 900 °C. The vertical dashed line indicates the divide between 700 °C isothermal cycles performed before and after high temperature exposure. Uncertainty bars are included for S_{H_2} but not S_{CO}, since the latter were negligible.

Table 1 S_{CO} and S_{H_2} during POM over CeO$_2$ and Ni–CeO$_2$ at 700–1100 °C. Uncertainty for S_{CO} values were negligible and thus are not included in the table

T (°C)	700	800	900	1000	1100
CeO$_2$ S_{CO}	N/A	0.99	0.98	0.97	0.96
Ni–CeO$_2$ S_{CO}	0.99	0.99	0.98	0.97	0.96
CeO$_2$ S_{H_2}	N/A	0.98 ± 0.02	0.98 ± 0.01	0.95 ± 0.01	0.90 ± 0.01
Ni–CeO$_2$ S_{H_2}	0.88 ± 0.07	0.85 ± 0.04	0.84 ± 0.01	0.81 ± 0.01	0.81 ± 0.01

deviations $\leq 1\%$ of the measured values. S_{CO} remains high (≥ 0.98) for the duration of testing, with no noticeable change following high temperature cycling at 900 °C. Greater uncertainty and variability are seen for S_{H_2}, with the latter likely due to slight changes in pressure within the mass spectrometer over the course of the long experiments. Small deviations in pressure can result in significant changes to n_{H_2O} (eqn (6)) and even lead to negative values for n_{H_2O}, resulting in $S_{H_2} > 1.0$. However, these values are included for the sake of understanding overall trends. In total, average S_{H_2} is high at 0.98 and no noticeable trends with cycle number or post-high temperature cycling are apparent.

Additionally, SEM imaging and EDS element mapping were completed for LP Ni–CeO$_2$ before and after the 200 CLRM cycles at 700 °C to investigate dispersion of the Ni particles before and after cycling. Results of this characterization, shown in Fig. S4,† indicate metallic Ni is initially spread across the surface but with large clumps on the order of μm in some areas. Following 200 CLRM cycles at 700 °C, the large clumps are no longer present. Instead, small Ni particles are still spread across the surface with dense concentrations on singular CeO$_2$ particles of 100–1000 nm.

CLRM in a packed-bed reactor

Representative CLRM cycles. Consistently high X_{CH_4} and syngas selectivity are observed during POM for all cycles conducted in the packed bed configuration with LP Ni–CeO$_2$. Exemplary gas flow rates for 5 cycles completed at 700 °C are shown in Fig. 6. Starting from the left, no CH$_4$ is measured leaving the reactor at the beginning of the first POM reaction, indicating X_{CH_4} ~ 1.0. As time progresses, X_{CH_4} slowly decreases, as indicated by the increase in $\dot{n}_{CH_4}$. Note however, that $\dot{n}_{CH_4}$ for all times remains well below $\dot{n}_{CH_4,in}$. Product gases leaving the reactor consist primarily of $\dot{n}_{H_2}$ and $\dot{n}_{CO}$, but $\dot{n}_{CO_2}$ is also present at the start of the reaction before decreasing below the detection limit.

Conversion of CO$_2$ (X_{CO_2}) is high at the start of each oxidation and decreases only after most of the solid is fully oxidized. This is evidenced by negligible $\dot{n}_{CO_2}$ for the first ~ 5 min of the reaction, followed by the rapid increase of $\dot{n}_{CO_2}$ to $\dot{n}_{CO_2,in}$.

Interestingly, the peak in $\dot{n}_{CO}$ is significantly higher than the rate of CO$_2$ conversion, which is a result of the carbon deposition during POM and its subsequent oxidation in this step. This is because for every mole of carbon oxidized with CO$_2$, 2 moles of CO are produced, as shown in eqn (16).

$$C\ (s) + CO_2 \rightarrow 2CO \qquad (16)$$

We assume the solid CeO$_2$ oxidizes fully, thus the amount of carbon removed during this step can be determined from $\dot{n}_{CO}$. Total carbon deposited during POM, determined using eqn (15), and removed during oxidation are equivalent within the calculated range of uncertainty, indicating negligible accumulation of carbon over a complete cycle. Following the first cycle, the remaining four cycles are characterized by narrower peaks in $\dot{n}_{H_2}$ and $\dot{n}_{CO}$ during POM, presumably because some of the yields in the first cycle were due to reduction of NiO to Ni following exposure to air during startup. The yields and rates all remain constant for the last four cycles where only metallic Ni is likely present, and therefore only these cycles are considered in further data analysis.

Comparison to CeO$_2$

Fig. 7 shows the time response of X_{CH_4}, $\dot{n}_{H_2}$, $\dot{n}_{CO}$, and $\dot{n}_{CO_2}$ (subplots a–d, respectively) over a range of temperatures during POM over LP Ni–CeO$_2$ and LP CeO$_2$. Temperatures were kept below 800 °C for Ni–CeO$_2$ but were higher for CeO$_2$, between 900 °C and 1100 °C, because the reaction rates were negligibly slow at lower temperatures. In general, X_{CH_4} over Ni–CeO$_2$ at $T \leq$ 800 °C are comparable to CeO$_2$ at $T = 1100$ °C. As seen in Fig. 7a, $X_{CH_4} \sim 1.0$ for the first 2 minutes at the lowest temperature of 700 °C and 3.5 minutes at 800 °C using Ni–CeO$_2$. When compared to CeO$_2$, analogous behavior was only seen at the highest operating temperature of 1100 °C. For POM over CeO$_2$ at 900 °C and 1000 °C, lower X_{CH_4} is observed. For example, at 1000 °C, X_{CH_4} starts at 1.0 but decreases quickly after 0.5 min to $X_{CH_4} = 0.7$ and stays relatively constant for the remaining time shown. At 900 °C, X_{CH_4} is initially very low, near 0.4, then decreases further and stays constant at $X_{CH_4} = 0.22$ for the
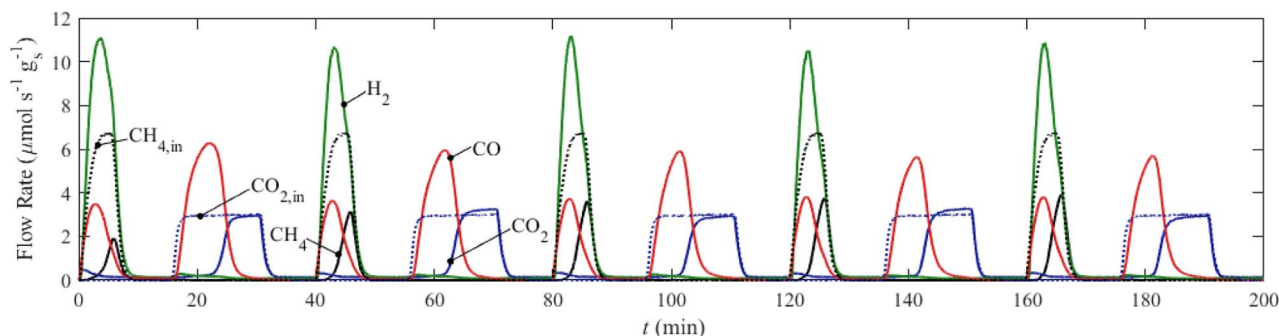

Fig. 6 Exemplary specific gas flow rates during five consecutive CLRM cycles over LP Ni–CeO$_2$ in a packed-bed tube reactor. Cycles were performed at 700 °C with $\nu_g = 0.135$ m s^{-1}. Specific flow rates are displayed as measured and are not corrected for dispersion. Operating conditions for each step are: (reduction) $\Phi_{CH_4} = 10$ vol% balanced in Ar for $t_{red} = 5$ min; (purge) $\Phi_{Ar} = 100$ vol% for $t_{purge} = 10$ min; (oxidation) Φ_{CO_2} $= 5$ vol% balanced in Ar for $t_{ox} = 15$ min.
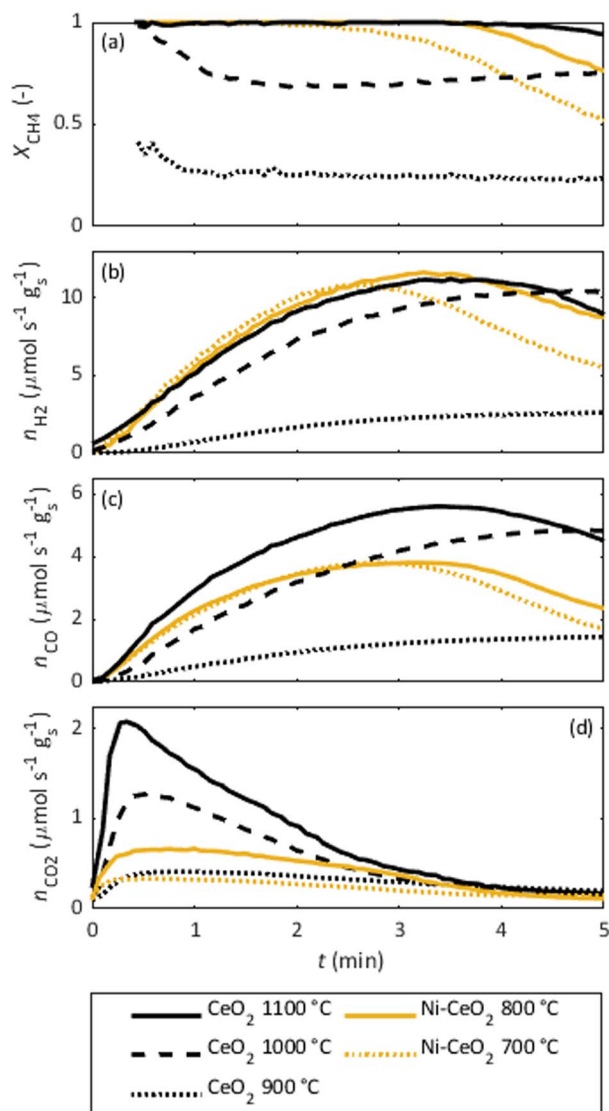
Fig. 7 Time response curves during POM over CeO_2 at 1100 °C, 1000 °C, and 900 °C and Ni–CeO_2 at 800 °C and 700 °C: (a) X_{CH_4}, (b) $\dot{n}_{H_2}$, (c) $\dot{n}_{CO}$, and (d) $\dot{n}_{CO2}$. All curves are taken from the final cycle completed at each set of conditions and are not corrected for dispersion. v_g and Φ_{CH_4} were held constant at 0.135 m s^{-1} and 10 vol%, respectively.

remainder of the reaction. For CeO_2 at 800 °C, X_{CH_4} was too low to quantify.

$\dot{n}_{H_2}$ is nearly identical for CeO_2 at 1100 °C, Ni–CeO_2 at 800 °C, and Ni–CeO_2 at 700 °C at short times and matches expected trends based on the response of X_{CH_4}. Interestingly, $\dot{n}_{CO}$ does not follow the same trend and instead demonstrates greater rates at high temperature for CeO_2 compared to Ni–CeO_2. This is due to lower selectivity of all carbon containing product species to CO during the POM step when Ni–CeO_2 is used as the redox material. Indeed, a molar balance on carbon containing atomic species, described in eqn (15), confirms greater quantities of carbon deposition over Ni–CeO_2, in agreement with high rates of carbon formation seen in other work.[29,30] However, since $\dot{n}_{CO2}$ decreases over the course of the reaction while $\dot{n}_{CO}$ remains relatively high, selectivity of the carbon containing gas species (i.e. excluding solid carbon) to CO should increase as the POM reaction proceeds.

A summary of $\bar{X}_{CH_4}$ and total specific moles of products evaluated over the first 5 minutes of POM is shown in Fig. 8. As seen, POM over Ni–CeO_2 produces relatively high $\bar{X}_{CH_4}$ of 0.71 and 0.86 at 700 °C and 800 °C, respectively. Comparable results are only achieved for CeO_2 at $T \geq 1000$ °C. At lower temperatures, $\bar{X}_{CH_4}$ was much lower, reaching only 0.06 at 800 °C. Total H_2 and CO production follow roughly the same trend as $\bar{X}_{CH_4}$; i.e., comparable yields to Ni–CeO_2 are only present for CeO_2 at the highest temperatures of 1000 °C and 1100 °C, but with notably higher H_2/CO ratios during POM over Ni–CeO_2. These higher H_2/CO ratios (i.e. H_2/CO > 2) result primarily from greater quantities of carbon deposition. Coking is negligible over CeO_2 at all operating T during the first 5 min of POM; in contrast, 435 and 530 μmol g$_s^{-1}$ of carbon formation are observed for Ni–CeO_2 at 700 °C and 800 °C, respectively. However, according to mass balance calculations on the oxidation step, all carbon formed during POM is completely oxidized to form additional CO via the reaction shown in eqn (16). Thus, the total amount of CO produced during a full cycle with Ni–CeO_2 is not affected by carbon deposition, and the H_2/CO ratio over a complete CLRM cycle will be approximately 1 : 1. CO_2 production is relatively low compared to the total amount
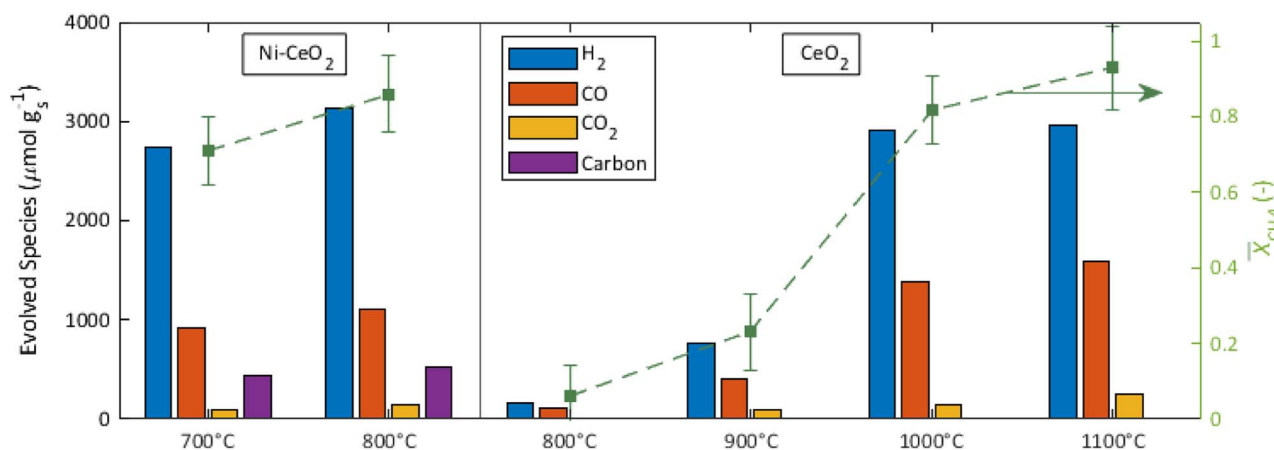

Fig. 8 Total specific moles of products and $\bar{X}_{CH_4}$ during the first 5 min of POM over LP Ni–CeO_2 or LP CeO_2 at various operating T.
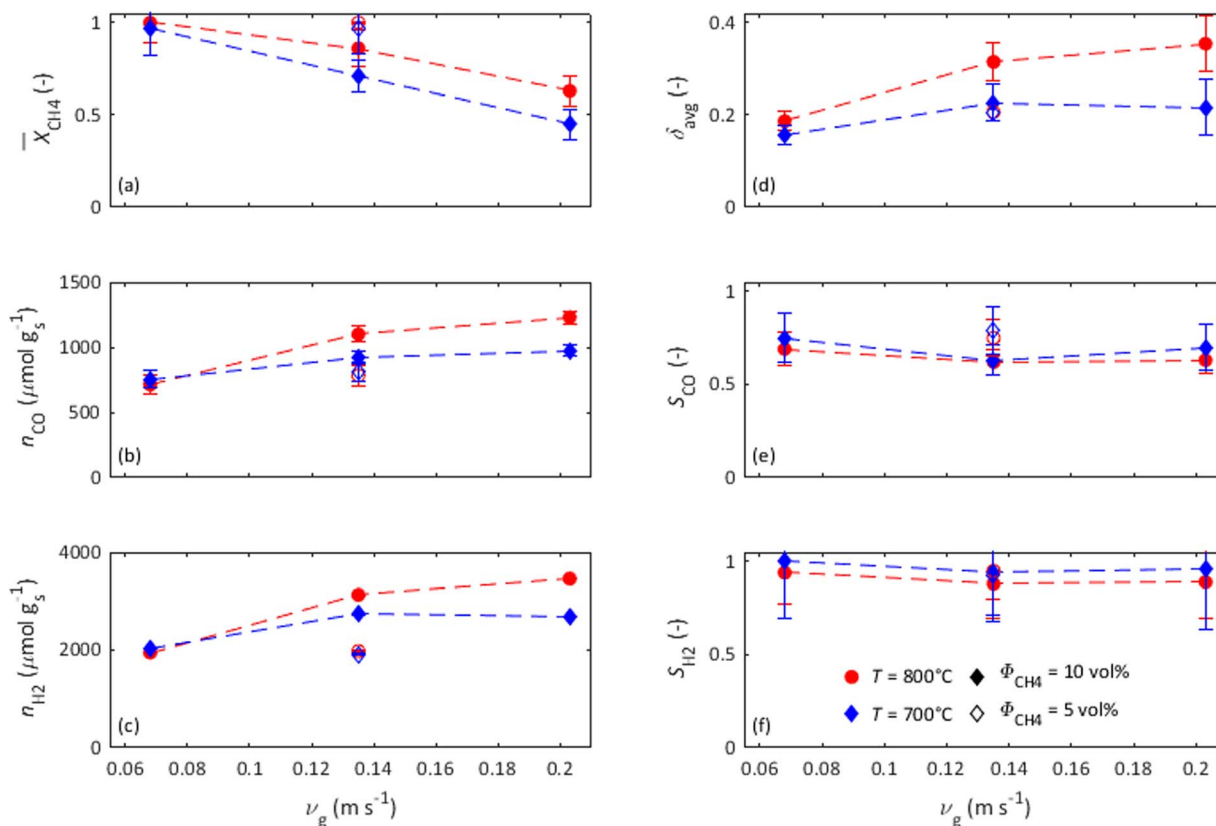
Fig. 9 Characterization of reactor performance after 5 minutes of POM over LP Ni–CeO$_2$ at the following operating conditions: $T = 800$ °C (red) or $T = 700$ °C (blue) and $\Phi_{CH_4} = 10$ vol% (solid) or $\Phi_{CH_4} = 5$ vol% (empty). (a) $\bar{X}_{CH_4}$, (b) n_{CO}, (c) n_{H_2}, (d) δ_{avg}, (e) S_{CO}, and (f) S_{H_2} are plotted versus ν_g.

of syngas produced in all cases, and also decreases with decreasing temperature. Because CeO$_2$ experiments consisted of longer POM steps due to slower reaction rates, a tanks-in-series model was implemented for CeO$_2$ to correct for dispersion and accurately quantify total moles of each species produced during the first 5 min.

Parametric Study. Fig. 9 summarizes $\bar{X}_{CH_4}$, total syngas production (n_{CO} and n_{H_2}), final bed-averaged nonstoichiometry (δ_{avg}), and syngas selectivity (S_{H_4} and S_{CO}) after the first 5 min of POM for varied ν_g, T, and Φ_{CH_4}. Under all conditions, 5 CLRM cycles were completed with LP Ni–CeO$_2$ using the following exposure times: 5 min CH$_4$ delivery, 10 min Ar purge, 15 min CO$_2$ delivery, and 10 min Ar purge. Results are the average of the last 4 cycles. Notably, $\bar{X}_{CH_4}$ is nearly 1.0 at the lowest ν_g of 0.068 m s^{-1} but decreases to 0.63 and 0.45 at 800 °C and 700 °C, respectively, as ν_g increases to 0.203 m s^{-1}. Conversely, δ_{avg} and total moles of syngas produced, i.e. n_{CO} and n_{H_2}, generally increase with ν_g. Thus, higher quantities of syngas production and greater oxygen exchange can be achieved at higher ν_g, but at the expense of lower $\bar{X}_{CH_4}$. δ_{avg}, n_{CO}, n_{H_2}, and $\bar{X}_{CH_4}$ also increase with T at all ν_g investigated as a result of faster kinetics at 800 °C. Finally, $\bar{X}_{CH_4}$ increases with decreasing Φ_{CH_4}, whereas δ_{avg}, n_{CO}, and n_{H_2} all decrease.

S_{CO} and S_{H_2} are not significantly affected by changes in ν_g, and only a slight trend of increasing selectivity with decreasing T is present. S_{H_2} is also not affected by changes in Φ_{CH_4}, but S_{CO}

decreases with increasing Φ_{CH_4}. The CO/CO$_2$ ratio did not change notably under any conditions; however, carbon formation did increase significantly with Φ_{CH_4}. Decreases in S_{CO} are thus a reflection of a larger portion of converted methane depositing as carbon during the POM step as Φ_{CH_4} increases. As indicated previously, this carbon is readily oxidized during the CO$_2$ splitting step.

It is also important to note that all of the above results are compared for a fixed reaction time. Consequently, reaction times are not optimized for each condition. For example, as shown in Fig. 7, $X_{CH_4} \sim 1.0$ at the start of POM for $\nu_g = 0.135$ m s^{-1}; thus, limiting the reaction time could improve $\bar{X}_{CH_4}$. Others have demonstrated high conversions and selectivity for CLRM over Ni catalyzed CeO$_2$, but only for fixed ν_g and Φ_{CH_4}.[29,30] The results of this parametric study suggest the high conversions and selectivities reported in previous studies potentially came at the expense of lower ν_g and/or Φ_{CH_4}, and therefore lower total syngas production. By tuning operating conditions, simultaneous optimization of conversion, selectivity, and total syngas production should be possible.

Conclusions

In this study, CLRM over Ni catalyzed CeO$_2$ is characterized using thermogravimetry and compared directly to non-catalyzed CeO$_2$. The apparent E_a during POM over Ni–CeO$_2$ is

presented for the first time and remained below 50 kJ mol^{-1} for $\delta_{red} < 0.35$, before slowly increasing at higher δ_{red}. Notably, E_a is significantly lower for Ni–CeO$_2$ compared to CeO$_2$ at all δ_{red}. Extended cycling with Ni–CeO$_2$ in the TGA demonstrated stable reaction rates and yields during CLRM at 700 °C, and S_{CO} remained above 0.98 for the duration of experimentation.

Using a packed-bed reactor, direct comparison of CLRM at 800 °C confirmed significantly higher rates of syngas production with Ni–CeO$_2$ *versus* CeO$_2$. Overall performance, including methane conversion and total syngas production, with Ni–CeO$_2$ at low temperatures (*i.e.*, 700 °C and 800 °C) was comparable to CeO$_2$ when operating at higher cycling temperatures of 1000–1100 °C. The only notable difference observed for Ni–CeO$_2$ was a significant increase in carbon deposition during POM; however, the deposited carbon is easily oxidized to form additional CO in the subsequent CO$_2$ splitting reaction and does not affect the overall H$_2$/CO ratio. These results indicate promise for using Ni catalyzed CeO$_2$ to generate syngas at the same rate as unmodified CeO$_2$ CLRM systems but at notably lower operating temperatures. Further investigation is needed to determine the effect of Φ_{CH_4} at higher volume fractions, as well as the effect of increased pressure on CLRM with Ni–CeO$_2$. Future work should focus on filling in these gaps in our understanding, then extracting ideal operating conditions to optimize the rate of syngas production over Ni–CeO$_2$ in scalable and efficient reactor systems.

Author contributions

Caroline Hill: conceptualization, investigation, methodology, formal analysis, writing original draft; Rachel Robbins: investigation, formal analysis; Philipp Furler and Simon Ackermann: conceptualization, supervision; Jonathan Scheffe: funding acquisition, conceptualization, project administration, supervision, writing review & editing.

Conflicts of interest

Authors Philipp Furler and Simon Ackermann are employees of Synhelion SA, which provides funding for this work.

Acknowledgements

References

1 C. Agrafiotis, H. von Storch, M. Roeb and C. Sattler, *Renewable Sustainable Energy Rev.*, 2014, **29**, 656–682.

2 R. Schäppi, D. Rutz, F. Dähler, A. Muroyama, P. Haueter, J. Lilliestam, A. Patt, P. Furler and A. Steinfeld, *Nature*, 2022, **601**, 63–68.

3 M. E. Dry, *Catal. Today*, 2002, **71**, 227–241.

4 H. Schulz, *Appl. Catal., A*, 1999, **186**, 3–12.

5 F. Mueller-Langer, E. Tzimas, M. Kaltschmitt and S. Peteves, *Int. J. Hydrogen Energy*, 2007, **32**, 3797–3810.

6 M. Usman, W. M. A. Wan Daud and H. F. Abbas, *Renewable Sustainable Energy Rev.*, 2015, **45**, 710–744.

7 Z. Hou, P. Chen, H. Fang, X. Zheng and T. Yashima, *Int. J. Hydrogen Energy*, 2006, **31**, 555–561.

8 P. Djinović, I. G. O. Črnivec, J. Batista, J. Levec and A. Pintar, *Chem. Eng. Process.: Process Intensif.*, 2011, **50**, 1054–1062.

9 S. D. Angeli, G. Monteleone, A. Giaconia and A. A. Lemonidou, *Int. J. Hydrogen Energy*, 2014, **39**, 1979–1997.

10 R. F. Zheng and R. S. Wegeng, *Integrated Solar Thermochemical Reaction System (Final Report), Pacific Northwest National Lab. (PNNL)*, Richland, WA (United States), 2019.

11 J. R. Rostrupnielsen and J. H. B. Hansen, *J. Catal.*, 1993, **144**, 38–49.

12 P. Summa, B. Samojeden and M. Motak, *Pol. J. Chem. Technol.*, 2019, **21**, 31–37.

13 P. Furler, J. R. Scheffe and A. Steinfeld, *Energy Environ. Sci.*, 2012, **5**, 6098–6103.

14 W. C. Chueh and S. M. Haile, *Philos. Trans. R. Soc., A*, 2010, **368**, 3269–3294.

15 W. C. Chueh and S. M. Haile, *ChemSusChem*, 2009, **2**, 735–739.

16 S. Ackermann, L. Sauvin, R. Castiglioni, J. L. M. Rupp, J. R. Scheffe and A. Steinfeld, *J. Phys. Chem. C*, 2015, **119**, 16452–16461.

17 O. T. Sørensen, *J. Solid State Chem.*, 1976, **18**, 217–233.

18 K. J. Warren, J. Reim, K. Randhir, B. Greek, R. Carrillo, D. W. Hahn and J. R. Scheffe, *Energy Technol.*, 2017, **5**, 2138–2149.

19 S. Chuayboon, S. Abanades and S. Rodat, *Front. Energy Res.*, 2020, **8**, 128.

20 J. R. Fosheim, B. J. Hathaway and J. H. Davidson, *Energy*, 2019, **169**, 597–612.

21 K. J. Warren, R. J. Carrillo, B. Greek, C. M. Hill and J. R. Scheffe, *Energy Technol.*, 2020, **8**, 2000053.

22 M. Fathi, E. Bjorgum, T. Viig and O. A. Rokstad, *Catal. Today*, 2000, **63**, 489–497.

23 A. J. Carrillo, L. Navarrete, M. Laqdiem, M. Balaguer and J. M. Serra, *Mater. Adv.*, 2021, **2**, 2924–2934.

24 J. Guerrero-Caballero, T. Kane, N. Haidar, L. Jalowiecki-Duhamel and A. Löfberg, *Catal. Today*, 2019, **333**, 251–258.

25 C. Ruan, Z.-Q. Huang, J. Lin, L. Li, X. Liu, M. Tian, C. Huang, C.-R. Chang, J. Li and X. Wang, *Energy Environ. Sci.*, 2019, **12**, 767–779.

26 Y. Zhang, Y. Zhao, Q. Yi, G. Wei, L. Shi and H. Zhou, *Fuel Process. Technol.*, 2021, **219**, 106875.

27 Z. Cao, X. Zhu, K. Li, Y. Wei, F. He and H. Wang, *Chem. Eng. J.*, 2020, **397**, 125393.

28 M. Ouyang, P. Boldrin, R. C. Maher, X. Chen, X. Liu, L. F. Cohen and N. P. Brandon, *Appl. Catal., B*, 2019, **248**, 332–340.

29 A. Löfberg, J. Guerrero-Caballero, T. Kane, A. Rubbens and L. Jalowiecki-Duhamel, *Appl. Catal., B*, 2017, **212**, 159–174.

30 Y. Han, M. Tian, C. Wang, Y. Kang, L. Kang, Y. Su, C. Huang, T. Zong, J. Lin, B. Hou, X. Pan and X. Wang, *ACS Sustainable Chem. Eng.*, 2021, **9**, 17276–17288.

31 K. J. Warren and J. R. Scheffe, *Mater. Today Energy*, 2018, **9**, 39–48.

32 C. M. Hill, E. A. Hernaiz, P. Furler, S. Ackermann and J. R. Scheffe, *Energy Technol.*, 2022, **10**, 2100473.

33 R. J. Carrillo, K. J. Warren and J. R. Scheffe, *J. Sol. Energy Eng.*, 2019, **141**, 021007.